Better understand the crystallization dynamics of ZrCu TFMGs: Benefits of combining global and local in situ approaches

Solène Comby-Dassonneville, Lucian Roiban, Alejandro Borroto, Annie Malchère, Sandrine Cardinal, Thierry Douillard, Cyril Langlois, J.F. Pierson, Jean-marc Pelletier, Philippe Steyer

Better understand the crystallization dynamics of ZrCu TFMGs: benefits of combining global and local in situ approaches

Solène Comby-Dassonneville[1,2], Lucian Roiban[1], Alejandro Borroto[3,4], Annie Malchère[1], Sandrine Cardinal[1], Thierry Douillard[1], Cyril Langlois[1], Jean-François Pierson[3], Jean Marc Pelletier[1], Philippe Steyer[1]

1 Univ Lyon, INSA Lyon, Université Claude Bernard Lyon 1, CNRS, MATEIS, UMR5510, 7 avenue Jean Capelle, 69621 Villeurbanne, France

2 Current position : Aix Marseille Univ, Université de Toulon, CNRS, IM2NP, Marseille, France

3 Université de Lorraine, CNRS, IJL, F-54000 Nancy, France

4 Current position : Univ Rennes, CNRS, IETR-UMR 6164, F-35000 Rennes, France

Abstract

This work describes crystallization mechanisms in a model ZrCu thin film metallic glass, synthesized through magnetron sputtering. Global-scale characterization techniques, including differential scanning calorimetry and X-ray diffraction, are compared with local-scale characterization obtained through *in situ* transmission electron microscopy during isothermal heating. This multi-scale approach establishes the crystallization sequence of ZrCu thin film metallic glasses. Furthermore, it highlights the role of oxidation as a nucleation site, initiating the crystallization process. Once initiated, crystallization progresses as a propagating front, scanning and transforming the amorphous matrix. The combination of both global and local approaches yields consistent key thermodynamic values. Additionally, monitoring the advancing crystallization front during in situ high-temperature transmission electron microscopy provides access to crucial kinetic parameters, such as diffusion coefficients.

Keywords

Thin films; metallic glasses; crystallization; *in situ* TEM; thermal stability

1. Introduction

The amorphous state of metallic glasses (MGs) and their overall chemical homogeneity, provide them with unique properties, such as outstanding mechanical properties with large elastic domains and high hardness, as well as excellent corrosion resistance. This makes metallic glasses materials of great interest for various applications such as biomedical [1-4], sports and luxury [5, 6] or various other industrial applications [7]. Thus, since their discovery in the 1960s [8], metallic glasses have been widely studied. The main part of published works on MGs is related to bulk materials [2, 3, 5-10], but there has been a recent increasing interest in thin film metallic glasses (TFMGs) [1, 4, 11-16]. Indeed, due to the rapid cooling rate from the liquid state required to obtain a MG, only relatively small pieces of bulk material can be formed. This manufacturing can be facilitated by the use of multicomponent alloys involving a significant atomic size mismatch and negative heats of mixing [5, 7]. However, this results in highly specific multi-component bulk metallic glasses (BMG), with only little room for optimization of the chemical composition in view of targeted properties. In addition, the presence of multiple components may also pose biocompatibility issues, as in the case of Ni, which is often added in Zr-based BMGs [3]. As an alternative, physical vapor deposition (PVD) is associated with very high quenching rates (up to 10^9 $K.s^{-1}$) [17]. It allows the production of large areas of thin film metallic glasses

(TFMGs) with a wide range of accessible chemical compositions, even for model binary or ternary systems [4, 12].

Nevertheless, as out-of-equilibrium materials, the properties of MGs (bulk or thin) change significantly during heating. Thus, the ductility of MGs is highly enhanced above the glass transition temperature T_g. This allows the thermoplastic forming of MGs at high temperature, which provides access to the design of specific shapes of MGs or to surface patterning [6, 18, 19]. The low crystallization temperature of MGs can also be an advantage to obtain composites materials: a mixture of metallic glass with crystalline phases. This crystalline phase can either hinder the rapid propagation of shear bands, deflect the shear bands orientation away from the maximum shear direction, or act as preferential site for shear band initiation, resulting in the multiplication of shear bands [20, 21]. This modifies the toughness and the ductility of amorphous/crystalline composites. Outstanding properties of MGs are also observed under thermal cycling, with relaxation and rejuvenation mechanisms [22].

The study of the *in situ* thermal evolution of MGs is then a crucial point. In the literature, thermally activated phenomena of MGs, such as structural relaxation, glass transition or crystallization, have been studied using differential scanning calorimetry (DSC) [6, 23], dynamic mechanical analyses (DMA) [24], thermomechanical analyses (TMA) [24-26], X-ray diffraction (XRD) [23], and mechanical testing [5, 9, 23]. Although these techniques are well adapted to BMGs, the study of TFMGs is more problematic due to the small amount of material available, and thermal study are most often limited to X-ray diffraction and to DSC measurements [12, 14, 27]. These techniques allow structural characterization of TFMGs during heating at the global scale, and can give general trends on the crystallization kinetic. However, those techniques do not provide access to the real physical changes occurring locally in TFMGs.

In order to determine structural changes in TFMGs, new methodologies must be developed. A method based on high-temperature nanoindentation has recently been proposed to track structural transformations in materials [28]. It allowed the investigation of the metallic glass to supercooled-liquid transition as well as the crystallization in a model ZrCu TFMG [29]. However, this study, which relies on monitoring of mechanical properties, is carried out indirectly, without any direct observation of the microstructural evolution. Within the past few years, several studies have been published on direct *in situ* observations of physical changes in TFMGs using transmission electron microscopy (TEM) analyses [30-36]. Those studies were of great interest in visualizing chemical heterogeneities upon heat treatment below the crystallization temperature [31], identifying the observed crystallized phases [36] or to investigating different crystallization steps or grain growth in multicomponent Au-, Zr-, Al-, Fe- or Pd-based BMGs [30, 32-35].

The aim of this paper is to propose a dual analysis combining macroscopic and local scales, to enhance the understanding of the transformation mechanisms from the metallic glass state to the crystallized state in a ZrCu TFMG. For this purpose, characterizations recorded at the macroscale through conventional global methods (DSC and XRD) are coupled with complementary local scale *in situ* TEM observations during an isothermal treatment at 400°C.

2. Experimental details

2.1 Thin film deposition

The ZrCu film was directly deposited onto various substrates using DC magnetron co-sputtering of Zr and Cu targets adopting a confocal configuration. The sputtering chamber was pumped down via mechanical and turbomolecular pumps allowing a base vacuum of 10^{-6} Pa. Prior to the deposition, substrates were sputter-etched using a radiofrequency plasma during 5 minutes. A rotating substrate holder was used to ensure good lateral homogeneity of the film composition and thickness. The target-to-substrate distance was fixed at 9 cm. Using a throttle valve, the deposition pressure was fixed to 0.5 Pa using an argon flow rate of 30 sccm. Zirconium and copper targets (50.8 mm diameter, 3 mm-thick,

and purity higher than 99.9%) were powered by a Maxim 1000 DC generator. A Cu content of 50 at% was targeted by applying target currents of 0.3 A to the Zr target and 0.056 A to the Cu one. The film was deposited without external heating. As expected, the chemical composition of the film, determined by EDX analysis, is $Zr_{51}Cu_{49}$. The vocable ZrCu will be deliberately used in the following text, to make more simple reading of the paper.

Substrates-free samples for DSC measurements were prepared by depositing the ZrCu TFMG onto sodium chloride (NaCl) substrates. Then the substrates were dissolved in distilled water, leaving the ZrCu TFMGs free-standing for analysis. For XRD analyses, 6 µm-thick ZrCu TFMGs were deposited onto amorphous silica. TEM observations were performed on 70 nm-thick ZrCu TFMGs deposited on a Nano-Chip from DENSsolutions for TEM observations [37].

2.2 Characterization methods

DSC measurements during non-isothermal testing were first performed to obtain key transformation parameters, such as the glass transition temperature (T_g) and the onset of crystallization temperature (T_x). Measurements were conducted with a Perkin Elmer DSC-7 under high-purity dry nitrogen at a flow rate of 20 mL.min^{-1} on 5 mg substrate-free samples from 30 to 550°C with two different rates (3 and 15 °C min^{-1}). Results for ZrCu-TFMGs have been provided in a previous work [29] and show a T_g of 385 °C and 395 °C for the 3 °C min^{-1} rate and the 15°C min^{-1} rate samples, respectively, and a T_x of 407 °C and 429°C. These results justify the choice of the selected isothermal temperature of this study (400°C), which is between T_g and T_x.

X-ray diffraction analyses during 400°C-isothermal heating were conducted using an AXS Bruker D8 Advance diffractometer with Cu K_α radiation (λ= 0.15406 nm) in Bragg–Brentano geometry, with an Anton Paar HTK 1200 oven chamber operating under vacuum (10^{-3} Pa). Locked coupled scans with 2θ from 27° to 47 ° were used during the isotherm, with a resulting duration of about 10 min for each measurement. Heating from room temperature to 400°C was carried out at the maximal heating rate of the device, *i. e.* 0.5 °C s^{-1}. Subsequently, the temperature was maintained at 400°C for 240 min. Cooling was performed at 0.5 °C s^{-1}.

In situ TEM observations during 400°C isothermal heating were conducted with an FEI-TITAN Cs-corrected eTEM operating at 300 kV under high vacuum (10^{-6} Pa). Heating was achieved using a MEMS-based sample holder from DENSsolutions. The isothermal temperature was reached in a few seconds, as was the room temperature after cooling. During the isotherm, TEM images were acquired every 30 s. Two samples were tested, in order to obtain two different magnifications (x4900 and x43000).

High resolution TEM (HR-TEM) was also performed after the heat treatment to determine the nature of crystallized phases. The detailed procedure for phase identification is given in supplementary information S1. This procedure is based on matching the fast Fourier transform (FFT) patterns of the experimental HR-TEM images with the theoretical diffraction patterns of potential phases using the CrystTBox software [38].

Furthermore, *post-mortem* observations of non-exposed sample areas were also performed, which showed no artifacts linked to a potential electron irradiation effect on the crystallization kinetic of ZrCu-TFMG (see supplementary information S2).

3. Results and discussion

3.1 Global-scale characterization

Results obtained from XRD measurements during 400°C-isothermal heating are shown in Fig. 1a. Despite the vacuum level and due to the high affinity of Zr with oxygen, ZrCu-TFMG shows evidence of oxidation in the early stages of the heat treatment. The tetragonal zirconia (t-ZrO_2) is present from the beginning, with competition from its monoclinic form (m-ZrO_2), which appears after approximatively 15 min. This initial oxidation was also shown in the literature for similar TFMGs compositions [27].

Then, intermetallic crystallization starts around t = 36 min, which corresponds to the crystallization incubation time τ. The first intermetallic crystallized phase is the orthorhombic (bco) $Cu_{10}Zr_7$, which corresponds to the stable expected phase of ZrCu alloys at 400°C [14, 27]. A slight evidence of cubic (c) ZrCu is also seen from t = 60 min. This phase is unexpected, since the c-ZrCu is not stable below 715°C [39, 40]. However, evidence of this metastable phase has already been reported in the literature [29, 41, 42], and is associated with metallic glasses that are rapidly heated and quenched, or that exhibit a slow diffusion rate and high viscosity [41]. In a previous work from our group [29], this metastable phase was also observed under heating before it dissociates into stable bco-$Cu_{10}Zr_7$ and t-Zr_2Cu phases during a 450°C isothermal annealing.

Then, the intensity of bco-$Cu_{10}Zr_7$ diffraction peaks increases from t = 36 min to t = 93 min, suggesting that crystallization fraction of bco-$Cu_{10}Zr_7$ increases up to t = 93 min. From this time, diffraction peaks do not significantly evolve anymore, which indicates that crystallization has stopped, despite a remaining amorphous hump at the end of the heating.

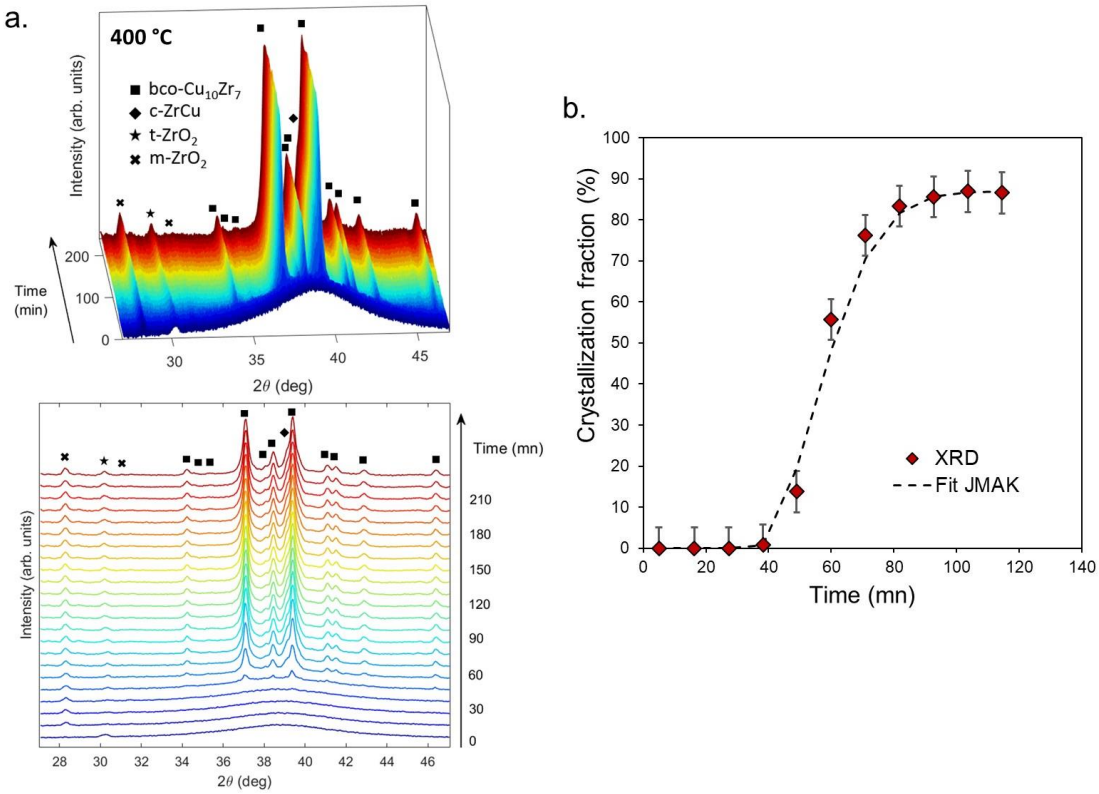

FIG 1: (a) *In situ* X-ray diffractogram of a ZrCu-TFMG during isothermal heating at 400°C at 10^{-3} Pa with 3D view (top) and 2D view (bottom) of all diffractograms from different time put together and (b) associated crystallization fraction against time with corresponding JMAK fit.

From the diffractograms, assuming that the bco-$Cu_{10}Zr_7$ is the highly preponderant phase, the crystallization fraction F_x can be estimated using Eq. 4, with I_a and I_x the integrated intensity of the amorphous hump and the crystallization phases, respectively [43, 44]. Results are shown in Fig. 1b, and

they are fitted using JMAK's modeling described in supplementary information S3. The total crystallization fraction at the end of the heat treatment is 87±3%.

$$F_x = \frac{I_x}{I_x + I_a} \quad (4)$$

Fig. 2 shows the local activation energy against the crystallization fraction (details on the calculation of the local activation energy can be found in supplementary information S3). The activation energy is roughly constant during the whole crystallization process, with a value at a crystallization fraction of 50% of $E_a \sim 440$ kJ mol^{-1}. This value is in good agreement with the values found in literature for similar compositions of ZrCu bulk metallic glasses [45].

The Avrami exponent and the reaction rate are found to be 1.9 +/- 0.1 and 6.2 +/-0.1·10^{-4} s^{-1}, respectively. Kinetics values from XRD measurements are summarized in Tab. 1. These values can be compared with values obtained from non-isothermal DSC measurements, using the analysis described in supplementary information S4, and shown in Tab. 1 and in Fig. 3. Although crystallization kinetics are not expected to be the same during isothermal and dynamic tests, close value of Avrami exponents are found. It suggests that crystallization would be governed by similar mechanisms during non-isothermal testing. Activation energies of the same order of magnitude can also be calculated.

The interpretation of the value of the Avrami exponent values was extensively discussed in literature. An approximation of the Avrami exponent is often given as $n = a + mb$, with $m = 0.5$ for volume-controlled crystallization (parabolic growth), *i. e.* if the crystallization is entirely controlled by long-range diffusion; and $m = 1$ for interface-controlled crystallization (linear growth) [6, 45 ,46, 47]. The b coefficient stands for the dimension of the particle growth, and thus is 3 for 3-dimentional growth, 2 for 2-dimentional growth and 1 for 1-dimentional growth. The a coefficient corresponds to the nucleation kinetics: its value is 0 when all the nuclei are already present, and no significant formation of new nuclei occurs during crystallization; 1 when the nucleation rate is constant during the whole crystallization; above 1 for increasing nucleation rate and below 1 for decreasing nucleation rate. However, another analytical derivation from Ilshner [48] gives an Avrami exponent n between 1 and 1.2 for volume-controlled crystallization of 3-dimentional particles with zero nucleation rate and $n = 1.7$ in case of constant nucleation rate. It also has to be noted that those analytical derivations are proposed for the crystallization of a unique phase, and the concurrent or successive crystallization of several phases may still make the interpretation of the Avrami exponent more challenging.

In the present case, an Avrami exponent close to 2 can be interpreted either as a crystallization driven by a volume-controlled growth of 3-dimentional particles or as an interface-controlled crystallization of 2-dimentional particles; both with a rapidly decreasing nucleation rate or no nucleation rate. Thus, the XRD data, alone, cannot be considered sufficient to solve the ambiguity involved in the crystallization mechanisms.

TAB. 1: Kinetics information extracted from XRD and TEM measurements. For comparison purpose, results from non-isothermal DSC measurements analyzed with the Various Heating Hate (VHR) method and the Kissinger–Akahira–Sunose (KAS) method are also shown (more details in supplementary information S4).

		τ (min)	E_a (kJ.mol^{-1})	Avrami exponent	K_0 (s^{-1})	K (400°C) (s^{-1})

XRD	400°C isotherm	36	445	1.9 +/- 0.1	2.2 +/- 0.1 · 10^{31}	6.2 +/- 0.1·10^{-4}
TEM	400°C isotherm	25	441	2.2 +/- 0.1	1.6 +/- 0.1 · 10^{31}	9.3+/- 0.1·10^{-4}
DSC (VHR)	3 °C/min	-	493	1.8 +/- 0.1	3.0 +/- 0.1 · 10^{34}	1.5 +/- 0.1·10^{-4}
	15 °C/min	-		1.8 +/- 0.1	3.0 +/- 0.1 · 10^{34}	1.5 +/- 0.1·10^{-4}
DSC (KAS)	3 °C/min	-	354	2.3 +/- 0.1	3.8 +/- 0.2 · 10^{23}	3.2 +/- 0.1·10^{-4}
	15 °C/min	-		2.2 +/- 0.2	7.2 +/- 0.1 · 10^{23}	6.0 +/- 0.1·10^{-4}

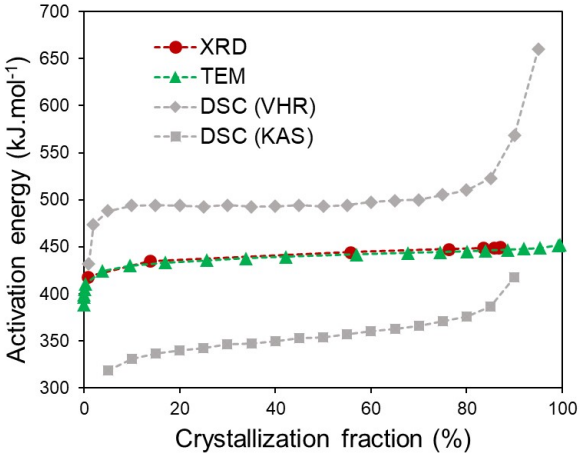

FIG. 2: Local activation energy obtained from XRD and TEM measurements during 400°C-isothermal heating. For comparison purpose, results obtained from non-isothermal DSC measurements analyzed with the Various Heating Hate (VHR) method and the Kissinger–Akahira–Sunose (KAS) method are shown (more details in supplementary information S4).

3.2 Local-scale characterization

Although XRD measurements provide macroscopic information about crystallization, *in situ* TEM observations can bring new insights on the understanding of crystallization mechanisms at a complementary deeper local scale.

Fig. 3a-l shows the low magnification microstructural evolution of the film as a function of the annealing time. Crystallized areas are identified by the manually-adjusted yellow selections in Fig. 3. At this magnification, first crystallization nuclei are found around t = 19 min. (Fig. 3b). Then, the number of crystallization nuclei increases until t = 29 min (Fig. 3c) where significant grain growth initiates. Crystallization seems to be completed around t = 60 min, and the sample does not evolve further until the end of the heat treatment. The crystallization fraction can be roughly estimated at each time step, as shown in Fig. 3m. The same approach as for XRD is applied, in order to deduce the Avrami exponent, the reaction rate, the incubation time and the activation energy for crystallization. All results are gathered in Tab. 1.

Although crystallization occurs at an equivalent time-scale compared to XRD measurements, it has to be noted that crystallization starts in advance during *in situ* TEM, with τ = 25 min, compared to τ = 36 min during HT-XRD. However, it is worth mentioning that this incubation time is obtained from the JMAK modeling of the crystallization fraction against the time. In fact, crystallization nuclei are clearly visible at TEM before this incubation time, around t = 19 min. Indeed, the incubation time would rather correspond to the time at which significant grain growth occurs, but crystallization nucleation may initiate much earlier, as shown by TEM observations. As comparison, XRD probably fails to properly

detect those crystallization nuclei due to their small sized distribution and the detection limit of the technique.

During *in situ* TEM, crystallization also appears to occur faster than during XRD experiments. Thus, both the Avrami exponent and the reaction rate obtained from TEM observations are slightly higher than for XRD measurements. However, the values remain of the same order, suggesting that the crystallization mechanism is similar. Besides, TEM observations reveal a first incubation time where nucleation happens, followed by the growth of crystallized areas without evidence of concurrent nucleation. This is consistent with a strongly decreasing nucleation rate during the grain growth.

Finally, the activation energy estimated from TEM experiments is similar to the activation energy value deduced from HT-XRD, as shown in Fig. 2. It also suggests that mechanisms would be the same for both experiments, despite their different probed surface over volume ratios. This result is particularly noteworthy considering the substantial difference in vacuum levels between the two experimental conditions (10^{-3} Pa versus 10^{-6} Pa).

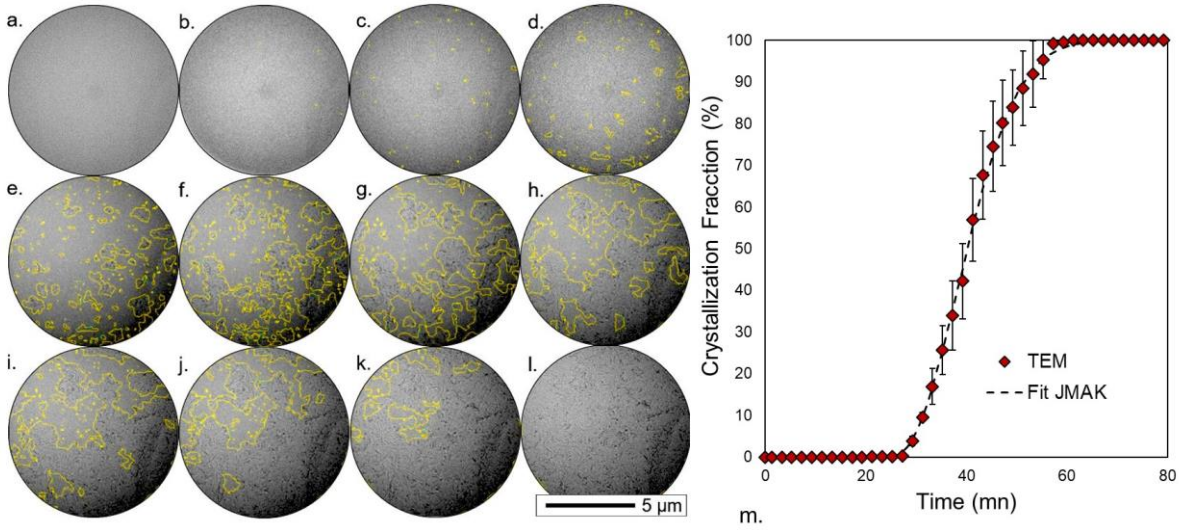

Fig. 3: Bright-field TEM micrographs of ZrCu-TFMG at low spatial resolution during 400°C heating at t = 0 min (a), t = 19 min (b), t = 24 min (c), t = 29 min (d), t = 34 min (e), t = 39 min (f), t = 41 min (g), t = 44 min (h), t = 47 min (i), t = 49 min (j), t = 54 min (k) and t = 60 min (l). Crystallized zones are identified by yellow highlighted areas, assuming a 100% crystallization after grain growth. Associated crystallization fraction against time and corresponding JMAK fit is given in (m). Full film in supporting information.

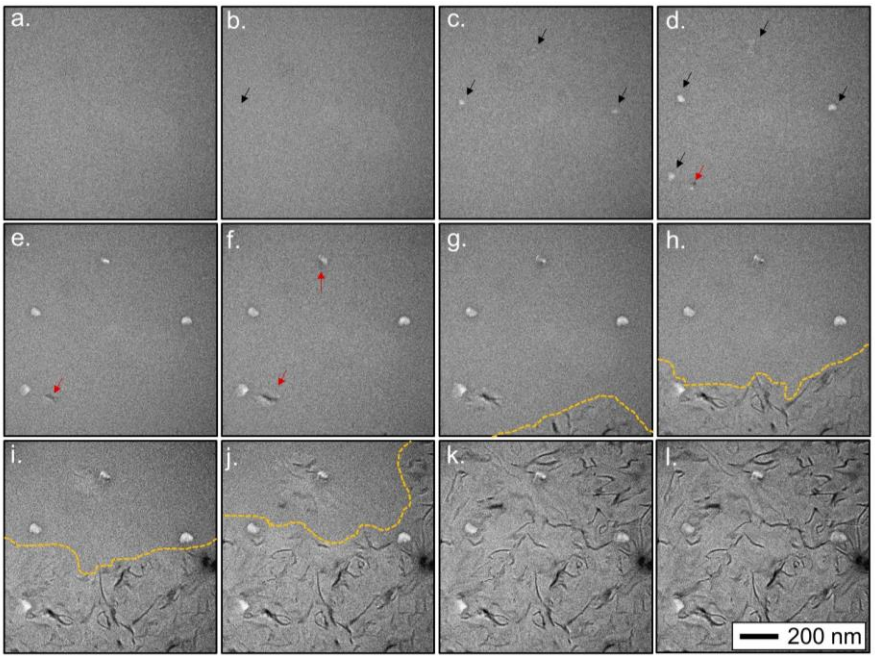

FIG. 4: TEM images of ZrCu-TFMG during 400°C heating at t = 0 min (a), t = 2 min (b), t = 9 min (c), t = 19 min (d), t = 29 min (e), t = 34 min (f), t = 39 min (g), t = 44 min (h), t = 47 min (i), t = 49 min (j), t = 54 min (k) and t = 60 min (l). The main crystallization front is highlighted in yellow. Full film in supporting information.

In order to obtain further complementary information on crystallization mechanisms, observations are also performed at a higher magnification, as shown in Fig. 4. These images reveal that precipitates with light contrast appear 2 min after the beginning of the heat treatment (black arrays in Fig. 4b-d). HR-TEM performed after heating on those particles allows their identification as m-ZrO_2 (Fig. 5a). Thus, as for XRD, oxidation occurs prior to the crystallization of intermetallic precipitates.

Then, a region with dark filament-like contrasts (bottom red arrays in Fig. 4d-f) appears at t = 19 min. Its contrast is close to that observed in Fig. 3, which suggests that it could correspond to a crystallization nucleus. A second crystallization nucleus appears at t = 34 min (top red array in Fig. 4f). It is worth mentioning that both nuclei nucleate in close vicinity of zirconia precipitates. This could corroborate the idea that zirconia precipitates would favor the crystallization, as suggested in a previous work by Apreteusei *et al*. [27]. Indeed, since zirconium atoms are used to produce Zr-rich precipitates, the vicinity around zirconia precipitates is supposed to be enriched in Cu. These Zr-depleted zones would be sites where nucleation of Cu-rich phases may initiate (*e.g.* bco-Zr_7Cu_{10} phase, as indicated by XRD characterization).

Finally, Fig. 4 shows evidences of crystallization growth. First, the bottom nucleus slightly grows before being covered by a fast crystallization front, characterized by dark river-like patterns among a middle-grey matrix, that propagates from the bottom to the top of the picture between t = 39 min and t = 54 min (Fig. 4f-k). Thus, the time-scale is compatible with the grain growth step observed in Fig. 3. The top nucleus remains roughly stable up to t = 49 min, and then starts to grow. This growth could be either due to the growth of the nucleus itself or caused by the propagation of the crystallization front within the volume of the film.

The analysis of the *post-mortem* HR-TEM images after heating has confirmed the presence of the bco-Zr_7Cu_{10} as the preponderant intermetallic phase. In particular, this phase was found in the dark river-like pattern of Fig. 4, as shown in Fig. 5 b. The middle-grey matrix around those river-like patterns corresponds to poorly-oriented regions, with some FFT dots compatible with bco- $Cu_{10}Zr_7$. Interestingly, some regions of this matrix also remain in an amorphous state (Fig. 5 c). It has to be noted that this

remaining amorphous region is consistent with the resulting amorphous hump observed after XRD experiments.

The fast propagation of the crystallization front is really similar to the eutectic reaction observed in several metallic glasses [42, 49]. This rather suggests a crystallization driven by an interfacial growth instead of a volume-controlled growth. It has to be noted that in case of interface-controlled crystallization, the Avrami exponent, which was found to be around 2 for both TEM and XRD results, appear to be rather weak. It might indicate a 2-dimentional growth of particles, instead of a 3-dimentional growth, due to the thin film nature of the sample and despite the large micrometric thickness of the deposited layer for XRD measurements. Interestingly, in the present work, the formed crystals after the front propagation are mainly Zr_7Cu_{10}, with some evidence of ZrCu observed by XRD, and with a remaining amorphous phase confirmed by XRD and observed between the dark river-like patterns by TEM. This behavior is close to the observation of a so-called pseudo-eutectic reaction found by Bazlov et al. [50] in a Al-based metallic glass at slow heating rate. For such pseudo-eutectic reaction a remaining amorphous phase was also observed around the intermetallic compounds after the passing of the crystallization front, and thus without common boundary between intermetallic compounds. In this case, the Avrami exponent was rather low for 3-dimensional interface-controlled growth. Thus, this pseudo-eutectic reaction could also be responsible for a weak Avrami exponent.

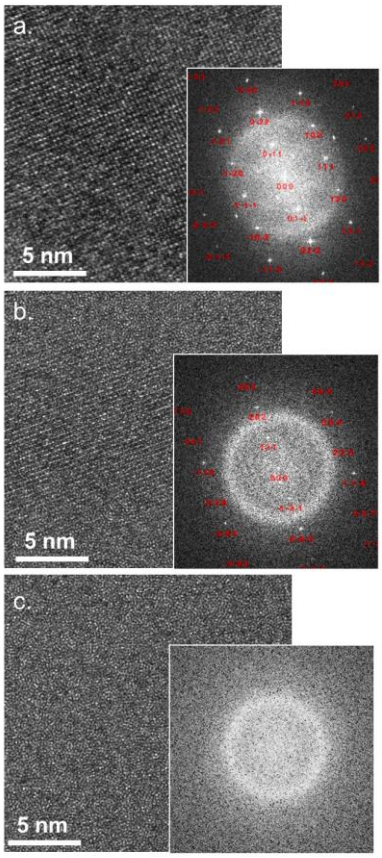

FIG. 5: Example of indexation of (a) the m-ZrO_2 (zone axis [-2,1,1]) and (b) the bco-Zr_7Cu_{10} phase (zone axis [17,-7,4]). Evidence of remaining amorphous phase is shown in (c).

Finally, the displacement rate v of the bottom-to-top crystallization front can be measured from each TEM image. This displacement rate v is found roughly constant with time, and is estimated to be around

0.7 ± 0.1 nm.s^{-1}. This is highly consistent with an interfacial-controlled crystallization, which is characterized by a linear growth of the crystallized particles.

Assuming that the diffusion required to separate the different phases of the pseudo-eutectic reaction occurs ahead of the crystallization front, and since the investigated temperature is far below the melting temperature, Eq. 5 can be used to estimate the diffusion coefficient at 400°C [51]. In this equation, λ corresponds to the distance between two lamellaes of the pseudo-eutectic products. In the present case, only the Zr_7Cu_{10} phase have been successively indexed by TEM, and λ was measured as the mean distance between two dark river-like patterns and estimated to be of the order of 100nm. As a result, a diffusion coefficient D around 3.10^{-17} m² s^{-1} was deduced. This diffusion coefficient most likely stands for copper diffusion in the amorphous ZrCu, since it has been shown in literature from both experimental work and molecular dynamic simulation that below 1.2 T_g, the diffusion is mostly controlled by the atom size [52- 55].

$$v \propto \frac{4D}{\lambda} \quad (5)$$

A value of D within the 10^{-17} m² s^{-1} order of magnitude is similar to the values found in the literature for the diffusion of solute atoms with atomic radii sizes close to that of Cu (Fe, Co, Ni) in Zr-based metallic glasses and supercooled liquids [56- 59], or in binary systems such as CoZr [58, 60, 61], NiZr [62] or FeZr [58, 63]. However, the direct comparison with values from the literature should be carefully considered since the diffusion coefficient may not only depend on the chemical composition, but also on the atomic packing of the metallic glass [54, 58].

4. Conclusion

In this study, a dual approach involving two complementary scales of investigation, global vs *in situ* local, was used in order to better understand the dynamics of crystallization for a model Zr-Cu TFMG. The crystallization mechanisms of ZrCu-TFMGs can be described as follows:

(i) Firstly, oxidation occurs, with nucleation of well-defined zirconia precipitates. Such behavior has been proved by XRD at a global scale, as well as locally by TEM.

(ii) Secondly, nucleation of bco-Zr_7Cu_{10} intermetallic phase arises in the close vicinity of zirconia precipitates. It suggests that crystallization of bco-Zr_7Cu_{10} is favored by the oxidation and may be caused by a chemical effect around the precipitates (with rich-Cu and poor-Zr regions).

(iii) The following crystallization itself is then illustrated by a fast displacement of a transformation front of bco-Zr_7Cu_{10} grains, which resembles a pseudo-eutectic transformation. However, at 400°C this crystallization front leaves a part of remaining amorphous untransformed matrix between the crystallized phases, revealed by both XRD and TEM technics.

From a quantitative point of view, really close crystallization kinetics were observed with our dual global-local approach, with close reaction rate ($6.2{\cdot}10^{-4}$ s^{-1} and $9.3{\cdot}10^{-4}$ s^{-1}, respectively) and Avrami exponents (1.9 and 2.2, respectively). Both measurements also give similar activation energies for crystallization (441 kJ.mol^{-1} and 445 kJ.mol^{-1}, respectively). It suggests that crystallization mechanisms are the same for both measurements, despite the different sample configurations (micrometric thin film for XRD *versus* nanometric thin film for TEM).

Both TEM and XRD techniques lead to comparable results in terms of crystallization kinetics. Besides, TEM analysis allowed to assess the presence of intermetallic nuclei much earlier than XRD

measurements. It also provided additional information on their sites of nucleation. Finally, it allowed for the measurement of a diffusion coefficient considering the continuous progression of the crystallization front.

Acknowledgement

The access to the FEI-TITAN eTEM was provided by the CLyM (Consortium Lyon Saint-Etienne de Microscopie: www.clym.fr) supported by the CNRS, the "GrandLyon" and the Rhône-Alpes Region (France). The Agence Nationale pour la Recherche (ANR-18-CE08-0018 MEGALIT) is greatly acknowledged for its financial support.

References

[1] P.H. Tsai, Y.Z. Lin, J.B. Li, S.R. Jian, J.S.C. Jang, C. Li, J.P. Chu, J.C. Huang, Sharpness improvement of surgical blade by means of ZrCuAlAgSi metallic glass and metallic glass thin film coating, Intermetallics. 31 (2012) 127–131. https://doi.org/10.1016/j.intermet.2012.06.014.

[2] M.S. Dambatta, S. Izman, B. Yahaya, J.Y. Lim, D. Kurniawan, Mg-based bulk metallic glasses for biodegradable implant materials: A review on glass forming ability, mechanical properties, and biocompatibility, Journal of Non-Crystalline Solids. 426 (2015) 110–115. https://doi.org/10.1016/j.jnoncrysol.2015.07.018.

[3] H.F. Li, Y.F. Zheng, Recent advances in bulk metallic glasses for biomedical applications, Acta Biomaterialia. 36 (2016) 1–20. https://doi.org/10.1016/j.actbio.2016.03.047.

[4] S. Comby-Dassonneville, T. Venot, A. Borroto, E. Longin, C. der Loughian, B. ter Ovanessian, M.-A. Leroy, J.-F. Pierson, P. Steyer, ZrCuAg Thin-Film Metallic Glasses: Toward Biostatic Durable Advanced Surfaces, ACS Appl. Mater. Interfaces. 13 (2021) 17062–17074. https://doi.org/10.1021/acsami.1c01127.

[5] A. Inoue, A. Takeuchi, Recent development and application products of bulk glassy alloys, Acta Materialia. 59 (2011) 2243–2267. https://doi.org/10.1016/j.actamat.2010.11.027.

[6] J.-M. Pelletier, J. Qiao, Metallic Glasses, in: J.D. Musgraves, J. Hu, L. Calvez (Eds.), Springer Handbook of Glass, Springer International Publishing, Cham, 2019: pp. 617–643. https://doi.org/10.1007/978-3-319-93728-1_18.

[7] W.H. Wang, Bulk Metallic Glasses with Functional Physical Properties, Advanced Materials. 21 (2009) 4524–4544. https://doi.org/10.1002/adma.200901053.

[8] W. Klement, R.H. Willens, P. Duwez, Non-crystalline Structure in Solidified Gold–Silicon Alloys, Nature. 187 (1960) 869–870. https://doi.org/10.1038/187869b0.

[9] C.A. Schuh, T.C. Hufnagel, U. Ramamurty, Mechanical behavior of amorphous alloys, Acta Materialia. 55 (2007) 4067–4109. https://doi.org/10.1016/j.actamat.2007.01.052.

[10] A.L. Greer, Metallic glasses…on the threshold, Materials Today. 12 (2009) 14–22. https://doi.org/10.1016/S1369-7021(09)70037-9.

[11] C.-Y. Chuang, J.-W. Lee, C.-L. Li, J.P. Chu, Mechanical properties study of a magnetron-sputtered Zr-based thin film metallic glass, Surface and Coatings Technology. 215 (2013) 312–321. https://doi.org/10.1016/j.surfcoat.2012.04.101.

[12] M. Apreutesei, P. Steyer, L. Joly-Pottuz, A. Billard, J. Qiao, S. Cardinal, F. Sanchette, J.M. Pelletier, C. Esnouf, Microstructural, thermal and mechanical behavior of co-sputtered binary Zr–Cu thin film metallic glasses, Thin Solid Films. 561 (2014) 53–59. https://doi.org/10.1016/j.tsf.2013.05.177.

[13] J.P. Chu, T.-Y. Liu, C.-L. Li, C.-H. Wang, J.S.C. Jang, M.-J. Chen, S.-H. Chang, W.-C. Huang, Fabrication and characterizations of thin film metallic glasses: Antibacterial property and durability study for medical application, Thin Solid Films. 561 (2014) 102–107. https://doi.org/10.1016/j.tsf.2013.08.111.

[14] P. Zeman, M. Zítek, Š. Zuzjaková, R. Čerstvý, Amorphous Zr-Cu thin-film alloys with metallic glass behavior, Journal of Alloys and Compounds. 696 (2017) 1298–1306. https://doi.org/10.1016/j.jallcom.2016.12.098

[15] E. Huszar, A. Sharma, L. Székely, R. Raghavan, B. Putz, T.E.J. Edwards, R. Spolenak, J. Michler, L. Pethö, Synthesis and mechanical properties of co-deposited W nanoparticle and ZrCuAg metallic glass thin film composites, Thin Solid Films. 773 (2023) 139822. https://doi.org/10.1016/j.tsf.2023.139822.

[16] M. Jain, A. Sharma, K. Pajor, K. Wieczerzak, N.M. della Ventura, X. Maeder, J.J. Kruzic, B. Gludovatz, J. Michler, Mechanical properties and thermal stability of thin film metallic glass compared to bulk metallic glass from ambient to elevated temperatures, Journal of Alloys and Compounds. 960 (2023) 170728. https://doi.org/10.1016/j.jallcom.2023.170728.

[17] Y. Liu, J. Liu, S. Sohn, Y. Li, J.J. Cha, J. Schroers, Metallic glass nanostructures of tunable shape and composition, Nat Commun. 6 (2015) 7043. https://doi.org/10.1038/ncomms8043.

[18] T. Xia, N. Li, Y. Wu, L. Liu, Patterned superhydrophobic surface based on Pd-based metallic glass, Appl. Phys. Lett. 101 (2012) 081601. https://doi.org/10.1063/1.4747327.

[19] M. Hasan, J. Schroers, G. Kumar, Functionalization of Metallic Glasses through Hierarchical Patterning, Nano Lett. 15 (2015) 963–968. https://doi.org/10.1021/nl504694s.

[20] J. Qiao, H. Jia, P.K. Liaw, Metallic glass matrix composites, Materials Science and Engineering: R: Reports. 100 (2016) 1–69. https://doi.org/10.1016/j.mser.2015.12.001.

[21] S.D. Feng, L. Li, K.C. Chan, L. Qi, L. Zhao, L.M. Wang, R.P. Liu, Control of shear band dynamics in Cu50Zr50 metallic glass by introducing amorphous-crystalline interfaces, Journal of Alloys and Compounds. 770 (2019) 896–905. https://doi.org/10.1016/j.jallcom.2018.08.192.

[22] J. Ketkaew, R. Yamada, H. Wang, D. Kuldinow, B.S. Schroers, W. Dmowski, T. Egami, J. Schroers, The effect of thermal cycling on the fracture toughness of metallic glasses, Acta Materialia. 184 (2020) 100–108. https://doi.org/10.1016/j.actamat.2019.11.046.

[23] W.H. Wang, C. Dong, C.H. Shek, Bulk metallic glasses, Materials Science and Engineering: R: Reports. 44 (2004) 45–89. https://doi.org/10.1016/j.mser.2004.03.001.

[24] J.C. Qiao, S. Cardinal, J.M. Pelletier, H. Kato, Insight on the process ability of bulk metallic glasses by thermo-mechanical analysis and dynamic mechanical analysis, Journal of Alloys and Compounds. 628 (2015) 357–363. https://doi.org/10.1016/j.jallcom.2014.12.166.

[25] T.W. Tang, Y.C. Chang, J.C. Huang, Q. Gao, J.S.C. Jang, C.Y.A. Tsao, On thermomechanical properties of Au–Ag–Pd–Cu–Si bulk metallic glass, Materials Chemistry and Physics. 116 (2009) 569–572. https://doi.org/10.1016/j.matchemphys.2009.04.032.

[26] T. Yamasaki, S. Maeda, Y. Yokoyama, D. Okai, T. Fukami, H.M. Kimura, A. Inoue, Viscosity Measurements of $Zr_{55}Cu_{30}Al_{10}Ni_5$ and $Pd_{40}Cu_{30}Ni_{10}P_{20}$ Supercooled Liquid Alloys by Using a

Penetration Viscometer, Materials Transactions. 46 (2005) 2746–2750. https://doi.org/10.2320/matertrans.46.2746.

[27] M. Apreutesei, P. Steyer, A. Billard, L. Joly-Pottuz, C. Esnouf, Zr–Cu thin film metallic glasses: An assessment of the thermal stability and phases transformation mechanisms, Journal of Alloys and Compounds. 619 (2015) 284–292. https://doi.org/10.1016/j.jallcom.2014.08.253.

[28] G. Tiphéne, P. Baral, S. Comby-Dassonneville, G. Guillonneau, G. Kermouche, J.-M. Bergheau, W. Oliver, J.-L. Loubet, High-Temperature Scanning Indentation: A new method to investigate in situ metallurgical evolution along temperature ramps, Journal of Materials Research. 36 (2021) 2383–2396. https://doi.org/10.1557/s43578-021-00107-7.

[29] S. Comby-Dassonneville, G. Tiphéne, A. Borroto, G. Guillonneau, L. Roiban, G. Kermouche, J.-F. Pierson, J.-L. Loubet, P. Steyer, Real-time high-temperature scanning indentation: Probing physical changes in thin-film metallic glasses, Applied Materials Today. 24 (2021) 101126. https://doi.org/10.1016/j.apmt.2021.101126.

[30] K. Chrissafis, M.I. Maragakis, K.G. Efthimiadis, E.K. Polychroniadis, Detailed study of the crystallization behaviour of the metallic glass Fe75Si9B16, Journal of Alloys and Compounds. 386 (2005) 165–173. https://doi.org/10.1016/j.jallcom.2004.05.062.

[31] N. Van Steenberge, A. Concustell, J. Sort, J. Das, N. Mattern, A. Gebert, S. Suriñach, J. Eckert, M.D. Baró, Microstructural inhomogeneities introduced in a Zr-based bulk metallic glass upon low-temperature annealing, Materials Science and Engineering: A. 491 (2008) 124–130. https://doi.org/10.1016/j.msea.2008.01.083.

[32] S. Lan, X. Wei, J. Zhou, Z. Lu, X. Wu, M. Feygenson, J. Neuefeind, X.-L. Wang, In-situ study of crystallization kinetics in ternary bulk metallic glass alloys with different glass forming abilities, Appl. Phys. Lett. 105 (2014) 201906. https://doi.org/10.1063/1.4901905.

[33] S. Sohn, Y. Jung, Y. Xie, C. Osuji, J. Schroers, J.J. Cha, Nanoscale size effects in crystallization of metallic glass nanorods, Nat Commun. 6 (2015) 8157. https://doi.org/10.1038/ncomms9157.

[34] A.I. Bazlov, N.Y. Tabachkova, V.S. Zolotorevsky, D.V. Louzguine-Luzgin, Unusual crystallization of Al85Y8Ni5Co2 metallic glass observed *in situ* in TEM at different heating rates, Intermetallics. 94 (2018) 192–199. https://doi.org/10.1016/j.intermet.2017.12.024.

[35] Yu.P. Ivanov, C.M. Meylan, N.T. Panagiotopoulos, K. Georgarakis, A.L. Greer, In-situ TEM study of the crystallization sequence in a gold-based metallic glass, Acta Materialia. 196 (2020) 52–60. https://doi.org/10.1016/j.actamat.2020.06.021.

[36] G.I. Nkou Bouala, A. Etiemble, S. Dassonneville, C.D. Loughian, C. Langlois, J.-F. Pierson, P. Steyer, Structural and microstructural evolution of amorphous Zr-Cu-Ag thin-film alloys under thermal constraint: An *in situ* approach, Journal of Alloys and Compounds. 851 (2021) 156908. https://doi.org/10.1016/j.jallcom.2020.156908.

[37] J.R. Jinschek, Advances in the environmental transmission electron microscope (ETEM) for nanoscale *in situ* studies of gas–solid interactions, Chem. Commun. 50 (2014) 2696–2706. https://doi.org/10.1039/C3CC49092K.

[38] Klinger, M. & Jäger, A. (2015). Crystallographic Tool Box (CrysTBox): automated tools for transmission electron microscopists and crystallographers. J. Appl. Cryst. 48 (2015) 2012–2018. https://doi.org/10.1107/S1600576715017252

[39] W. Gierlotka, K.-C. Zhang, Y.-P. Chang, Thermodynamic description of the binary Cu–Zr system, Journal of Alloys and Compounds. 509 (2011) 8313–8318. https://doi.org/10.1016/j.jallcom.2011.04.141.

[40] N. Zou, H.-J. Lu, P.-W. Gu, J.-Y. Wang, X.-K. Feng, J.-Y. Shen, Y.-L. He, L. Li, X.-G. Lu, Thermodynamic assessment and glass forming ability prediction of the Zr-Fe-Cu system, Calphad. 64 (2019) 175–184. https://doi.org/10.1016/j.calphad.2018.12.007.

[41] T. Yamamoto, Y. Yokoyama, T. Ichitsubo, H. Kimura, E. Matsubara, A. Inoue, Precipitation of the ZrCu B2 phase in Zr50Cu50–xAlx (x = 0, 4, 6) metallic glasses by rapidly heating and cooling, Journal of Materials Research. 25 (2010) 793–800. https://doi.org/10.1557/JMR.2010.0105.

[42] D.V. Louzguine-Luzgin, G. Xie, Q. Zhang, C. Suryanarayana, A. Inoue, Formation, Structure, and Crystallization Behavior of Cu-Based Bulk Glass-Forming Alloys, Metall Mater Trans A 41 (2010) 1664–1669. https://doi.org/10.1007/s11661-009-0087-8.

[43] P. Wesseling, B.C. Ko, J.J. Lewandowski, Quantitative evaluation of α-Al nano-particles in amorphous $Al_{87}Ni_7Gd_6$—comparison of XRD, DSC, and TEM, Scripta Materialia. 48 (2003) 1537–1541. https://doi.org/10.1016/S1359-6462(03)00127-1.

[44] S. Gravier, P. Donnadieu, S. Lay, B. Doisneau, F. Bley, L. Salvo, J.J. Blandin, Evaluation of the crystal volume fraction in a partially nanocrystallized bulk metallic glass, Journal of Alloys and Compounds. 504 (2010) S226–S229. https://doi.org/10.1016/j.jallcom.2010.05.008.

[45] Q. Gao, Z. Jian, J. Xu, M. Zhu, F. Chang, A. Han, Crystallization kinetics of the Cu50Zr50 metallic glass under isothermal conditions, Journal of Solid State Chemistry. 244 (2016) 116–119. https://doi.org/10.1016/j.jssc.2016.09.023.

[46] D. Okai, Y. Shimizu, N. Hirano, T. Fukami, T. Yamasaki, A. Inoue, Isothermal crystallization in supercooled liquid state for Ca50Mg22.5Cu27.5 metallic glass, Journal of Alloys and Compounds. 504 (2010) S247–S250. https://doi.org/10.1016/j.jallcom.2010.03.225.

[47] S. Ranganathan, M. Von Heimendahl, The three activation energies with isothermal transformations: applications to metallic glasses, J Mater Sci 16 (1981) 2401–2404. https://doi.org/10.1007/BF01113575.

[48] B. Ilschner, Das Zeitgesetz des Ausscheidens neuer Phasen in Mischkristallen, Archiv Für Das Eisenhüttenwesen 26 (1955) 59–62. https://doi.org/10.1002/srin.195502020.

[49] D.V. Louzguine-Luzgin, A. Inoue, Nano-Devitrification of Glassy Alloys, Journal of Nanoscience and Nanotechnology 5 (2005) 999–1014. https://doi.org/10.1166/jnn.2005.158.

[50] A.I. Bazlov, N.Y. Tabachkova, V.S. Zolotorevsky, D.V. Louzguine-Luzgin, Unusual crystallization of Al85Y8Ni5Co2 metallic glass observed in situ in TEM at different heating rates, Intermetallics 94 (2018) 192–199. https://doi.org/10.1016/j.intermet.2017.12.024.

[51] U. Köster, U. Herold, Crystallization of metallic glasses, in: H.-J. Güntherodt, H. Beck (Eds.), Glassy Metals I: Ionic Structure, Electronic Transport, and Crystallization, Springer, Berlin, Heidelberg, 1981: pp. 225–259. https://doi.org/10.1007/3540104402_10.

[52] H. Hahn, R.S. Averback, Dependence of tracer diffusion on atomic size in amorphous Ni-Zr, Phys. Rev. B. 37 (1988) 6533–6535. https://doi.org/10.1103/PhysRevB.37.6533.

[53] A. Bartsch, K. Rätzke, A. Meyer, F. Faupel, Dynamic Arrest in Multicomponent Glass-Forming Alloys, Phys. Rev. Lett. 104 (2010) 195901. https://doi.org/10.1103/PhysRevLett.104.195901.

[54] J.C. Qiao, Q. Wang, J.M. Pelletier, H. Kato, R. Casalini, D. Crespo, E. Pineda, Y. Yao, Y. Yang, Structural heterogeneities and mechanical behavior of amorphous alloys, Progress in Materials Science. 104 (2019) 250–329. https://doi.org/10.1016/j.pmatsci.2019.04.005.

[55] A. Annamareddy, P.M. Voyles, J. Perepezko, D. Morgan, Mechanisms of bulk and surface diffusion in metallic glasses determined from molecular dynamics simulations, Acta Materialia. 209 (2021) 116794. https://doi.org/10.1016/j.actamat.2021.116794.

[56] K. Knorr, M.P. Macht, H. Mehrer, Self-Diffusion in Bulk Metallic Glasses, MRS Online Proceedings Library. 554 (1998) 269–274. https://doi.org/10.1557/PROC-554-269.

[57] H. Ehmler, A. Heesemann, K. Rätzke, F. Faupel, U. Geyer, Mass Dependence of Diffusion in a Supercooled Metallic Melt, Phys. Rev. Lett. 80 (1998) 4919–4922. https://doi.org/10.1103/PhysRevLett.80.4919.

[58] F. Faupel, W. Frank, M.-P. Macht, H. Mehrer, V. Naundorf, K. Raetzke, H. Schober, s Sharma, H. Teichler, Diffusion in Metallic Glasses and Supercooled Melts, Reviews of Modern Physics. 75 (2003). https://doi.org/10.1103/RevModPhys.75.237.

[59] S.W. Basuki, A. Bartsch, F. Yang, K. Rätzke, A. Meyer, F. Faupel, Decoupling of Component Diffusion in a Glass-Forming $Zr_{46.75}Ti_{8.25}Cu_{7.5}Ni_{10}Be_{27.5}$ Melt Far above the Liquidus Temperature, Phys. Rev. Lett. 113 (2014) 165901. https://doi.org/10.1103/PhysRevLett.113.165901.

[60] W. Dörner, H. Mehrer, Tracer diffusion and thermal stability in amorphous Co-Zr and their relevance for solid-state amorphization, Phys. Rev. B. 44 (1991) 101–114. https://doi.org/10.1103/PhysRevB.44.101.

[61] P. Klugkist, K. Rätzke, S. Rehders, P. Troche, F. Faupel, Activation Volume of ^{57}Co Diffusion in Amorphous $Co_{81}Zr_{19}$, Phys. Rev. Lett. 80 (1998) 3288–3291. https://doi.org/10.1103/PhysRevLett.80.3288.

[62] P. Ehrhart, R.S. Averback, H. Hahn, S. Yadavalli, C.P. Flynn, Fast diffusion and nucleation of the amorphous phase in Ni–Zr films, Journal of Materials Research. 3 (1988) 1276–1278. https://doi.org/10.1557/JMR.1988.1276.

[63] J. Horváth, J. Ott, K. Pfahler, W. Ulfert, Tracer diffusion in amorphous alloys, Materials Science and Engineering. 97 (1988) 409–413. https://doi.org/10.1016/0025-5416(88)90084-5.